SCIENTIFIC REPORTS

OPEN

Received: 08 June 2016
Accepted: 01 November 2016
Published: 18 November 2016

Charge storage mechanisms of manganese oxide nanosheets and N-doped reduced graphene oxide aerogel for high-performance asymmetric supercapacitors

Pawin Iamprasertkun[1,2], Atiweena Krittayavathananon[1], Anusorn Seubsai[2], Narong Chanlek[3], Pinit Kidkhunthod[3], Winyoo Sangthong[4], Santi Maensiri[5], Rattikorn Yimnirun[5], Sukanya Nilmoung[6], Panvika Pannopard[7], Somlak Ittisanronnachai[7], Kanokwan Kongpatpanich[8], Jumras Limtrakul[8] & Montree Sawangphruk[1]

Although manganese oxide- and graphene-based supercapacitors have been widely studied, their charge storage mechanisms are not yet fully investigated. In this work, we have studied the charge storage mechanisms of K-birnassite MnO_2 nanosheets and N-doped reduced graphene oxide aerogel (N-rGO_{ae}) using an *in situ* X-ray absorption spectroscopy (XAS) and an electrochemical quart crystal microbalance (EQCM). The oxidation number of Mn at the MnO_2 electrode is +3.01 at 0 V vs. SCE for the charging process and gets oxidized to +3.12 at +0.8 V vs. SCE and then reduced back to +3.01 at 0 V vs. SCE for the discharging process. The mass change of solvated ions, inserted to the layers of MnO_2 during the charging process is 7.4 μg cm^{-2}. Whilst, the mass change of the solvated ions at the N-rGO_{ae} electrode is 8.4 μg cm^{-2}. An asymmetric supercapacitor of MnO_2//N-rGO_{ae} (CR2016) provides a maximum specific capacitance of ca. 467 F g^{-1} at 1 A g^{-1}, a maximum specific power of 39 kW kg^{-1} and a specific energy of 40 Wh kg^{-1} with a wide working potential of 1.6 V and 93.2% capacity retention after 7,500 cycles. The MnO_2//N-rGO_{ae} supercapacitor may be practically used in high power and energy applications.

Supercapacitors or electrochemical capacitors are energy-storage devices widely used in many high-power applications[1,2]. They have high specific power (~10 kW kg^{-1}) and long cycle life (up to 500,000 cycles)[3] when compared with batteries[4]. This is because the charge storage mechanisms of supercapacitors are mainly at the solid-liquid interface via electrochemical double layer capacitive (EDLC) and pseudocapacitive behaviors. On the other hand, the batteries store charges via redox reactions based on intercalation chemistry[5]. Improvement in the specific energy of the supercapacitors while keeping their high specific power and capacitance retention is therefore a focal point in the supercapacitor research area.

Supercapacitors are classified to be either symmetric or asymmetric depending on the materials used at the positive and negative electrodes. The difficulty in developing symmetric supercapacitor, which use the identical material at both positive and negative electrodes, is that a single material will only prefer either solvated positive

[1]Department of Chemical and Biomolecular Engineering, School of Energy Science and Engineering, Vidyasirimedhi Institute of Science and Technology, Rayong 21210, Thailand. [2]Department of Chemical Engineering, Kasetsart University, Bangkok 10900, Thailand. [3]Synchrotron Light Research Institute (Public Organization), 111 University Avenue, Muang District, Nakhon Ratchasima 30000, Thailand. [4]Department of Chemistry, Kasetsart University, Bangkok 10900, Thailand. [5]School of Physics, Institute of Science, Suranaree University of Technology, Nakhon Ratchasima 30000, Thailand. [6]Department of Applied Physics, Faculty of Sciences and Liberal Arts, Rajamangala University of Technology Isan, Nakhon Ratchasima 30000, Thailand. [7]Frontier Research Centre (FRC), Vidyasirimedhi Institute of Science and Technology, Rayong 21210, Thailand. [8]Department of Materials Science and Engineering, Vidyasirimedhi Institute of Science and Technology, Rayong 21210, Thailand. Correspondence and requests for materials should be addressed to M.S. (email: montree.s@vistec.ac.th)

or negative ions. The charge storage performance of the symmetric supercapacitor is therefore limited by the electrode where it can store less charge. To solve this problem, asymmetric supercapacitors (ASCs) using different materials at the positive and negative electrodes are of interest since they can provide higher charge storage performance with wider working potentials[6]. The maximum charge storage capacity of the ASCs can be finely tuned and achieved by using proper materials and compositions at positive and negative electrodes. Therefore, the recent effort has been devoted to developing the electrode materials of the advanced ASCs. Recently, the ASC of the polypyrrole nanotubes (positive electrode)//N-doped carbon nanotubes (negative electrode) can provide a wide working potential of 1.4 V, a specific energy of 28.95 Wh kg^{-1} with a specific power of 7.75 kW kg^{-1} and a cyclic stability of ca. 90% retention after 2,000 cycles[7]. The ASC of Ni–Co hydroxide@reduced graphene oxide//3D porous carbon exhibits a specific energy of 56.1 Wh kg^{-1} with 80% retention after 17,000 cycles[8]. Note, Ni and Co hydroxides are battery-like electrode materials. The ASC of the MnO_2 nanosheet//carbon fibers displays a specific capacitance of 87.1 F g^{-1} and a specific energy of 27.2 Wh kg^{-1} with 95% capacitance retention over 3,000 cycles[9]. The ASC of Fe_2N //TiN exhibits 5.4 Wh kg^{-1} and specific power of ca. 6.4 kW kg^{-1} with 98% capacity retention in 20,000 cycles[10]. The ASC based on Ti-doped Fe_2O_3@PEDOT//MnO_2 provides an energy density of 0.89 mWh cm^{-3} with about 85% retention capacitance after 6,000 cycles[11]. To further improve the charge storage performance of the ASCs, the positive and negative electrode materials with high ionic and electronic conductivities, porosity, and surface area are needed. In this work, new advanced ASCs have been fabricated using MnO_2 nanosheets and nitrogen-doped reduced graphene oxide aerogel (N-rGO_{ae}) as positive and negative electrodes, respectively.

Among transition metal oxide materials, MnO_2 is well recognized as a good candidate for the positive electrode due to its wide potential range in the positive side and high theoretical specific capacitance, high stability, low cost, abundance, and no environmental hazard[12–15]. Lee and Goodenough firstly presented that the amorphous $MnO_2.H_2O$ used as an active material for the supercapacitors in KCl solution exhibited a specific capacitance of ca. 200 F g^{-1} [16]. Toupin, M. *et al.* reported a change in the oxidation state between Mn^{3+} and Mn^{4+} during the charge/discharge process of the MnO_2 electrode using an *ex situ* X-ray photoelectron spectroscopy (XPS) measurement of the dried MnO_2 electrode after polarized[17]. They also reported that the charge compensation of the Mn^{3+} a reduced state is due to Na^+ and H^+ adsorption[17]. In contrast, Xu, C. *et al.* studied the charge storage mechanism of the MnO_2 by controlling the pH of the electrolytes and reported that the cations of the electrolyte rather than H^+ are responsible for the pseudocapacitance of MnO_2[18]. *In operando* Raman spectroscopy was also employed to probe the structural changes of the α-MnO_2 electrode during the charge/discharge process for which the charge storage mechanism is based on the intercalation chemistry[19]. As the results, it can be concluded here that the charge storage mechanisms of MnO_2-based supercapacitors are not yet fully clear.

Interestingly, the mixed valent MnO_x including MnO_2 and Mn_3O_4 recently reported exhibits superior charge storage performance than individual MnO_2 or Mn_3O_4[20–22]. Among several methods for the preparation of MnO_x nanostructures on conductive substrates including precipitation[23], sol-gel[16], and electrodeposition[24], the electrodeposition is well-recognized as an efficiency method with high homogeneity active species. It is also simple, scalable, and cheap technique[25]. Also, this technique does not require the polymer binders (e.g., PVDF, PTFE), which can introduce many disadvantages including an obstacle for the movement of ions and electronic charge transport. It is also necessary to note here that the charge storage mechanisms of the mixed valent MnO_x have not yet been investigated. Thus, understating how the Mn oxidation states do change during the charging/discharging processes is crucial to the development of this material.

For the negative electrodes, the N-rGO_{ae} with high surface area and porosity, which are good for supercapacitor electrodes. The diluted N- and O-containing groups of the N-rGO_{ae} can lead to high ionic adsorption[26]. They can also store the electronic charges via surface redox reactions[27,28]. Interconnected 3D graphene structure can enhance the diffusion of solvated ions via a capillary force providing ultrahigh specific powder[2]. However, an important question how much solvated ionic charges can be stored by the N-rGO_{ae} has not yet been reported. Electrochemical quartz crystal microbalance (EQCM) is then used in this work to address this issue during the charging/discharging processes.

In this work, MnO_2 nanosheets with a birnessite structure having negatively charged MnO_2 layers along with K^+ counter ions and water among the adjacent layers were synthesized by a potential-step electrodeposition. The oxidation number of Mn in MnO_2 nanosheets during the charging/discharging processes was subsequently monitored by an *in situ* X-ray absorption spectroscopy (XAS). In addition, the mass change on the electrodes of MnO_2 and N-rGO_{ae} during charging/discharging was evaluated by an *in situ* EQCM. The results provide further understanding on the charge storage mechanisms of MnO_2 nanosheets and N-rGO_{ae}.

Results and Discussion

Morphologies of as-synthesised materials. The morphology of the MnO_2 synthesized using the potential-step electrodeposition was characterized by FE-SEM as shown in Fig. 1a. The as-electrodeposited MnO_2 is rather porous with a pore diameter of ca. 10–50 nm due to the interconnection of the MnO_2 nanosheets. This morphology is ideal for the supercapacitor electrode since it can enhance the mass transport of the electrolyte due to the capillary force[29,30]. Figure 1b shows an FE-SEM image of N-rGO_{ae} illustrating a few layers of overlapping graphene sheets forming the framework structure with a pore diameter of 0.2–3 μm. The N-rGO_{ae} exhibits ultrahigh porosity, which can also accelerate the electrolyte diffusion on the negative electrode. Figure 1c displays a TEM image of the MnO_2 for which the morphology of the as-electrodeposited MnO_2 is a sheet-like shape with a diameter of ca. 20–50 nm. The MnO_2 nanosheets connect to each other forming a porous structure. Figure 1d shows a TEM image of N-rGO_{ae}, which is nearly transparent containing many wrinkles of the N-rGO_{ae} framework structure. In addition, the EDX mapping of the MnO_2 coated on the c-CFP substrate in Fig. 1e displays three main elements, which are C, O, and Mn with 40.2, 27.0, and 18.7% by atomic weight, respectively. The 14.1%

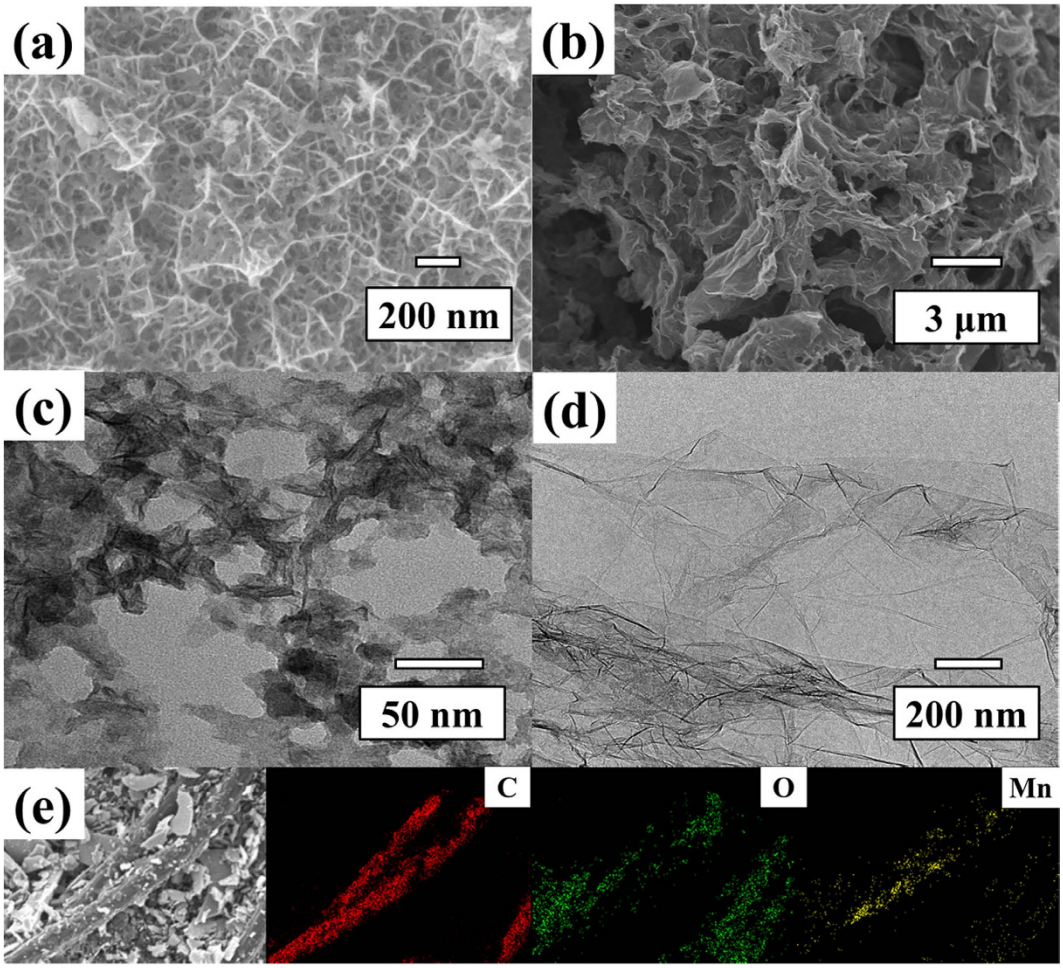

Figure 1. FE-SEM images of (**a**) MnO_2 and (**b**) N-rGO_{ae} as well as TEM images of (**c**) MnO_2 and (**d**) N-rGO_{ae} and (**e**) EDX mapping of MnO_2/c-CFP mainly containing C, O, and Mn elements.

remaining element is F, which comes from the carboxyl-modified carbon fiber paper (c-CFP) substrate since a PTFE is used as a binder in the production process of the CFP[13].

Structures of as-synthesised materials. To further study the physical and chemical properties of the as-synthesized materials, Raman, XRD, and XPS techniques were carried out. In Fig. 2a, Raman spectra of the MnO_2 display two main contribution peaks of the MnO_2. N-rGO_{ae} displays two distinct peaks at 1,350 and 1,580 cm^{-1} according to the normal characteristic peaks of the rGO materials. Generally, the D-band at 1,350 cm^{-1} represents the amount of the disordered carbon structure, which consists of the sp^3 carbon atoms at the edge of graphitic sheets. The G-band at 1,580 cm^{-1} illustrates the vibrational mode of the graphitic sp^2carbon sheets[31]. Additionally, the defect ratio (I_D/I_G) of N-rGO_{ae} is 1.05, which is in good agreement with other previous work[32]. The amorphous carbon content of N-rGO_{ae} calculated from the deconvoluted peaks at around 1,510 cm^{-1} is ca. 17.7%.

The XRD pattern of N-rGO_{ae} (Fig. 2b) displays two broad peaks at 2θ of 24.3 and 43.7° referring to the characteristics of rGO[33]. The XRD pattern of the as-electrodeposited MnO_2 indicates the K-birnessite MnO_2 nanosheets (JCPDS 80-1098)[34,35]. The peaks at 2θ about 12, 24, 37, 43, 56, and 66° are due to (0 0 1), (002), (111), (−112), (113), (020), and (220) planes showing a lamellar structure. The structure consists of single sheets of edge-sharing [MnO_6] octahedral and water molecules and K^+ between the adjacent layers[34–36]. The orthogonal distance between two consecutive slabs of [MnO_6] is ca. 7.3 Å. The mixed vacancy of manganese ions in K-birnassite MnO_2 nanosheets plays an important role of a spontaneous redox reaction enhancing the pseudocapacitance of ASCs[22]. In addition, the N_2 gas adsorption was carried out to determine the specific surface area and pore size distribution of N-rGO_{ae} as shown in Fig. 2c and d. By following the IUPAC classification, the gas adsorption isotherm of N-rGO_{ae} is in a type-IV isotherm (a hysteresis loop type II) owing to interconnected pore networks (see Fig. 2c). The BET surface area of N-rGO_{ae} is about 352 $m^2 g^{-1}$ having an average pore width of 3.7 nm (Fig. 2d).

Surface analysis of as-fabricated electrodes. The surface chemical composition of the as-fabricated electrodes was analyzed by the XPS technique. The C1s spectra of N-rGO_{ae} sprayed on c-CFP (Fig. 3a) display

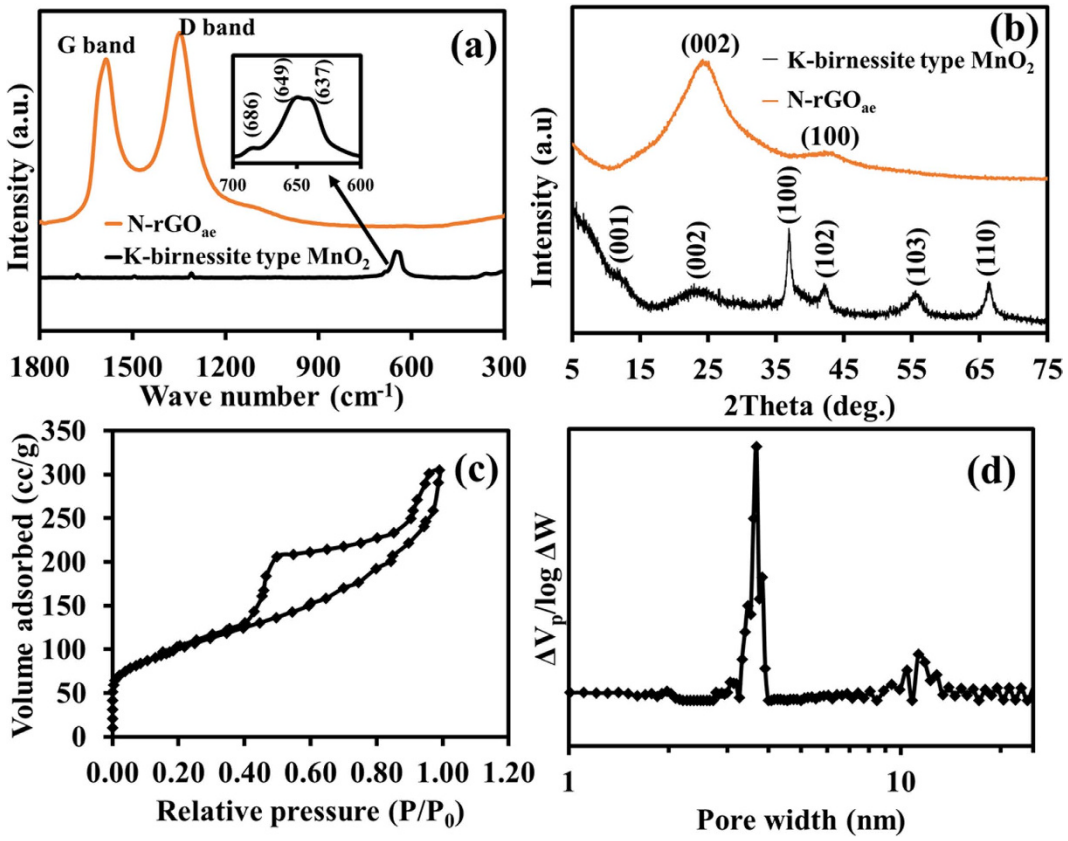

Figure 2. (**a**) Raman spectra, (**b**) XRD patterns of MnO_2 and N-rGO$_{ae}$ and (**c**) N_2 sorption isoterm and pore size distribution of N-rGO$_{ae}$.

four main peaks at 284.9, 285.2, 286.1, and 288.5 eV corresponding to C-C, C-N, C-O and C=O, respectively[37]. The diluted nitrogen content in Fig. 3b can be deconvoluted into four peaks of pyridinic N (399.8 eV), pyrolic N (400.5 eV), graphitic N (401.7 eV) and oxidized N (405.4 eV), respectively[38]. The graphitic N can improve the charge transfer in the rGO matrix[39]. Other N-functional groups (Pyrolic N and Pyridinic N) also play an important role for the pseudocapacitance[27,28,40].

A wide-scan XPS spectrum of MnO_2 coated on c-CFP is shown in Fig. 3c confirming the elements of the as-prepared electrode. Notably, K is also found on the XPS spectrum since K^+ is a balance charge of negatively-charged MnO_2 layers. The Mn2p spectra of the as-electrodeposited MnO_2 coated on c-CFP in Fig. 3d show two broad peaks of $Mn2p_{3/2}$ and $Mn2p_{1/2}$, which can be deconvoluted to many peaks corresponding to two different oxidation states of Mn species[41]. This material has the advantage of mixed valent MnO_2 for supercapacitors. Each broad peak can be classified into three parts at 640.9, 642.1, and 645.9 eV for $Mn2p_{3/2}$ and 652.6, 653.8, and 656.2 eV for $Mn2p_{1/2}$. The peaks at 640.9 and 652.6 eV are the characteristics of Mn^{3+} (21.3%) while those at 642.1 and 653.8 eV are the characteristics of Mn^{4+} (78.7%) as well as those at 645.9 and 656.2 eV are attributed to shakeup satellites. For the O1s XPS spectrum, which is not shown here, the spectrum contains three main peaks located at 531.4, 532.6, and 533.1 eV attributing to Mn-O-H, H-O-H and O-C, respectively[42].

Electrochemical evaluatioon of as-fabricated electrodes. To evaluate the electrochemical property of the as-fabricated electrodes, a three-electrode system using the as-synthesized material as a working electrode, a Pt wire as a counter electrode, and a saturated calomel electrode (SCE) as a reference electrode was carried out in 0.5 M Na_2SO_4 solution. The optimized potential range of the as-prepared electrodes is shown in CVs (Fig. 4a). Also, an optimum mass ratio finely tuned between the mass of active materials at positive and negative electrodes (m^+/m^-) is 1.75 providing the highest charge storage performance calculated by a charge balance according to Eq. 1[43] as follow;

$$\frac{m_+}{m_-} = \frac{C_{s-}\Delta V_-}{C_{s+}\Delta V_+} \quad (1)$$

where m is the mass of the active material, C_s is the specific capacitance, and ΔV is the voltage range for positive and negative electrodes[44]. Note, all electrochemical properties of half-cell MnO_2 and N-rGO$_{ae}$ electrodes are shown in Figure S1 and 2 of the supporting information, respectively. The MnO_2//N-rGO$_{ae}$ supercapacitor was then assembled using a hydrolyzed PE containing 0.5 M Na_2SO_4 as a separator. The operating potential window was varied from 0.8–1.6 V as shown in Fig. 4b. The rectangular-shaped CVs with a broad redox peak

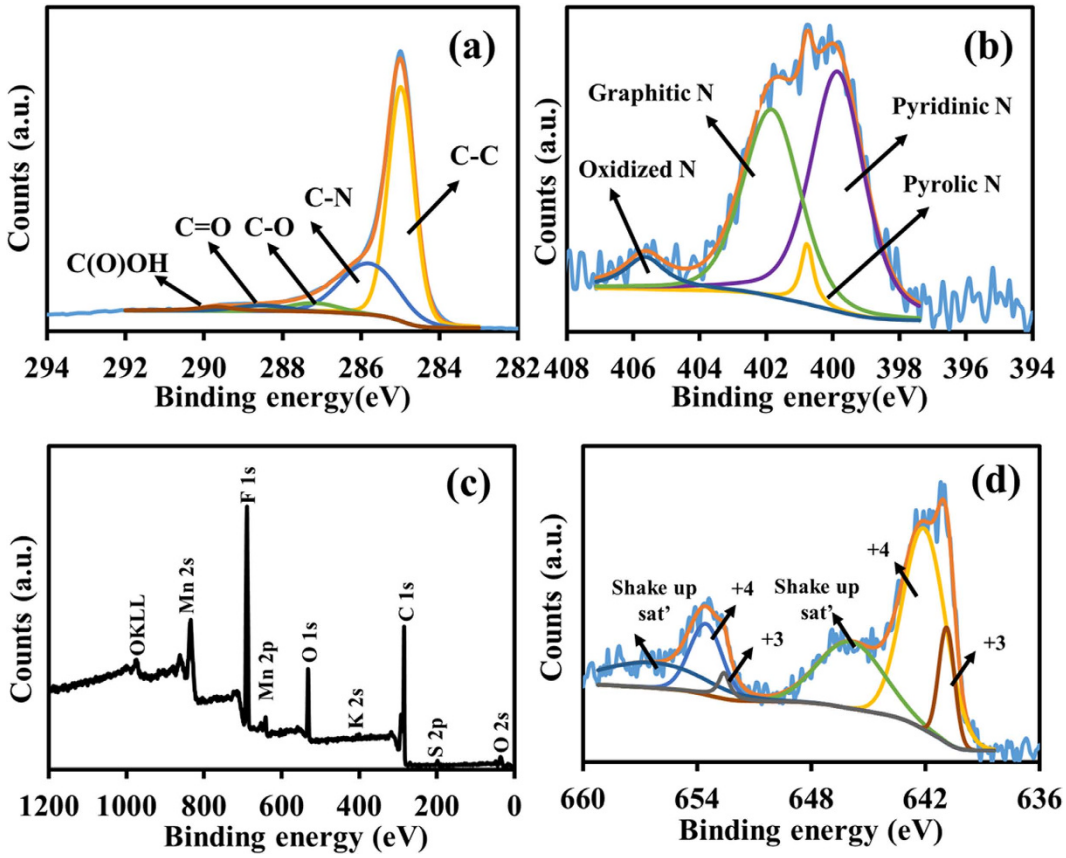

Figure 3. (**a**) C1s and (**b**) N1s XPS spectra of N-rGO$_{ae}$ on c-CFP, (**c**) XPS survey, and (**d**) Mn2p XPS of MnO_2.

indicate the pseudocapacitive behavior that comes from the surface redox reaction of MnO_2[15]. Surprisingly, the as-fabricated device levels off at the same range of the current density until 1.6 V. Moreover, GCDs show a symmetrical shape relating to the CV result (Fig. 4c). The MnO_2//N-rGO$_{ae}$ device exhibits the specific capacitances of 467.38–342.43 F g^{-1} (4.55–3.33 F cm^{-3}) at 1.0–5.0 A g^{-1}, respectively. The device has high coulombic efficiency up to 100% at 5 A g^{-1} (Fig. 4d). To further study the capacitive effect, b value was calculated from a power law according to Eq. 2[45] as follow;

$$i = av^b \tag{2}$$

where i is the current and ν is the scan rate. Both a and b are the constant parameters for which the b value can be determined from a slope of the linear plot between log i vs. log ν *(see inset graphs in* Fig. 4e and Figure S3a). According to power law relationship, i is equal to $a\nu$ for non-diffusion limited processes and i is equal to $a\nu^{1/2}$ for diffusion limited processes. Typically, the b value is equal to 1.0 for non-diffusion-controlled surface capacitive and equal to 0.5 for diffusion-controlled redox reaction, which is a typical battery behavior[44]. The result in Fig. 4e shows that the b values in this work are 0.56, 0.89, 0.95, 0.95, 0.84, 0.80 at the potentials of 0.25, 0.50, 0.75, 1.00, 1.25, and 1.50 V, respectively. This can confirm that the devices have both EDLC and surface redox reactions. In addition, the percentage of intercalation and capacitive contribution calculated by Eq. 3[46] is shown in Fig. 4f. The intercalation capacitance decreases when increasing scan rates due to the diffusion limit of the electrolytes.

$$I(V) = k_1 \mathrm{v} + k_2 v^{1/2} \tag{3}$$

where k_1 and k_2 are the slope and interception, respectively, which can be determined from Figure S3b.

Besides, the EIS result of the MnO_2//N-rGO$_{ae}$ supercapacitor at a sinusoidal signal of 10 mV from 100 kHz to 1 mHz is shown in the Nyquist plots (Fig. 5a). The straight line of the Nyquist plots increases sharply at a low frequency region to the Y-axis indicating almost the ideal supercapacitor dominated by the capacitive behavior from the formation of ionic and electronic charges. At high frequency, the electronic charge transfer resistance (R_{ct}) due to the surface redox of MnO_2 is about 13.45 Ω with an internal resistance (R_s) of 2.32 Ω located at the interception on the X-axis. In addition, the relaxation-time constant (τ_0), which is a minimum time required to discharge for all stored charges, can be determined from an inversion of the frequency at the maximum phase angle as shown in Fig. 5b. It is necessary to note the smaller value of τ_0 the higher power of the supercapacitors[47]. In this work, τ_0 is about 686 ms, which is much smaller than other previous report[1,48]. Finally, the stability of the MnO_2//N-rGO$_{ae}$ supercapacitor evaluated by the GCD method over 7,500 cycles at 5 A g^{-1} (Fig. 5c) is over 93.2% retention. The as-assembled device provides the highest specific energy of 40 Wh kg^{-1} and the highest specific

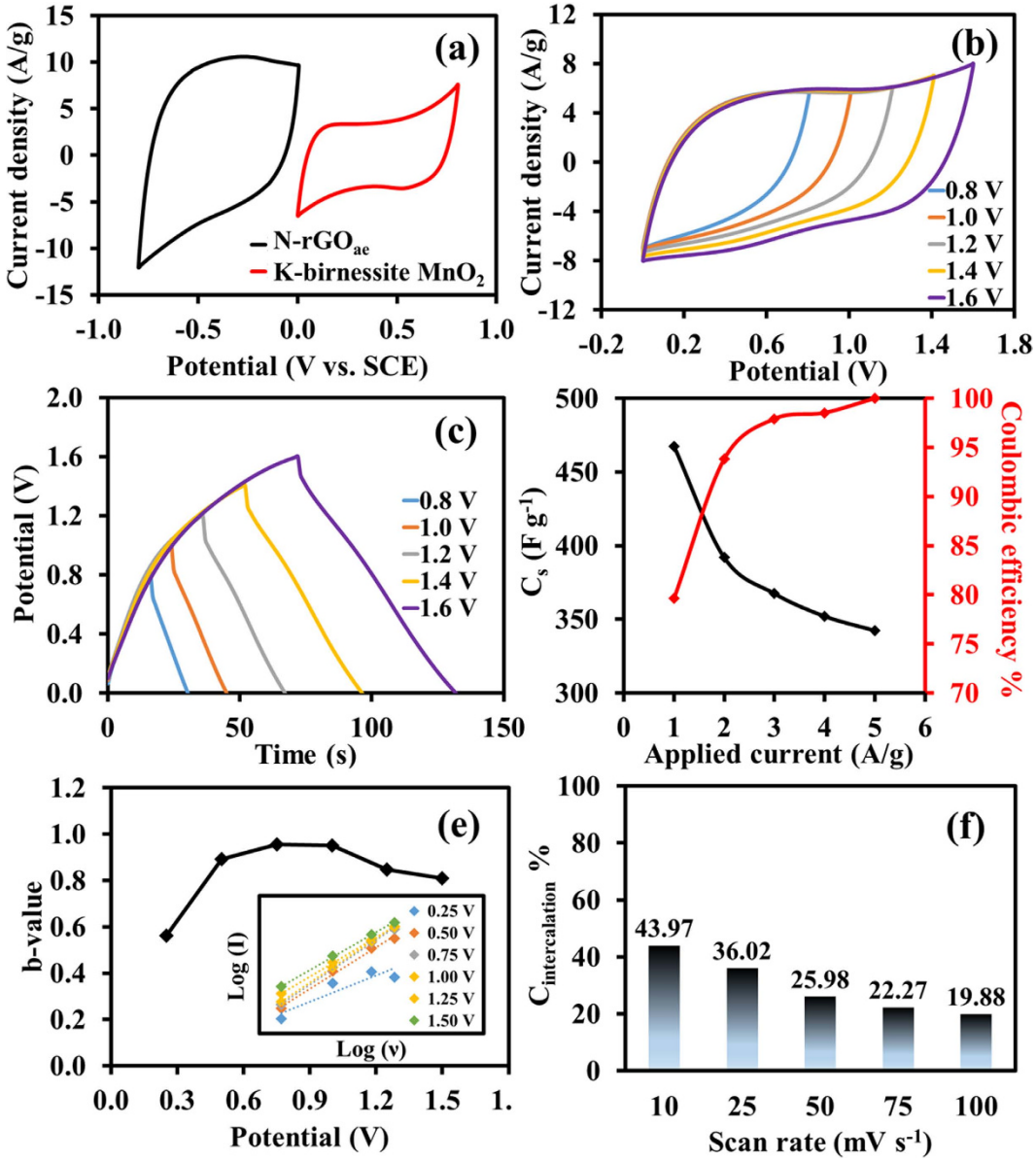

Figure 4. (**a**) CVs of the as-fabricated electrodes at 25 mV s^{-1} and (**b**) CVs at different working potentials (50 mV s^{-1}), (**c**) GCDs at different working potentials (5 A g^{-1}), and (**d**) specific capacitance and coulombic efficiency vs. applied current density, (**e**) the *b* value as a function of potential, and (**f**) the bar chart of the diffusion-controlled intercalation capacitance vs. scan rates of as-fabricated MnO_2//N-rGO$_{ae}$ supercapacitor devices.

power of 39 kW kg^{-1}, which are much higher than those of other previous related report (see Fig. 5d)[49–51]. Note, CVs at different scan rates, GVDs at different specific currents, and the calculated specific capacitances at different frequencies of the device are also shown in Figure S4 of the supporting information.

***In situ* X-ray absorption spectroscopy.** In order to clarify the origin of the remarkable specific energy and specific power of the MnO_2-based supercapacitor, the charge storage behavior occurred during the charge/discharge processes has been investigated by the *in-situ* XAS measurement. As Mn in the manganese oxide with different oxidation states plays a prominent role for the surface redox reaction during the charge/discharge process, *in situ* monitoring the oxidation number change of the Mn during charge/discharge processes is therefore crucial for understanding the pseudocapacitive behavior. In this work, the *in situ* XAS technique was carried out together with the chronoamperometry in 0.5 M Na_2SO_4 electrolyte during applying the potentials stepped from 0.0, 0.4, and 0.8 V vs. SCE and the backward potentials from 0.8 to 0.4 V vs. SCE and from 0.4 to 0.0 V vs. SCE. Note, in order to reach the steady state, each step potential was hold for 15 min before starting the XAS measurement[52,53]. The Mn K-edge fluorescence energy of the MnO_2 charged at 0.0 V vs. SCE is 6548.05 eV and the energy value increases up to 6548.36 and 6548.53 eV when the potentials were applied to 0.4 and 0.8 V vs. SCE, respectively

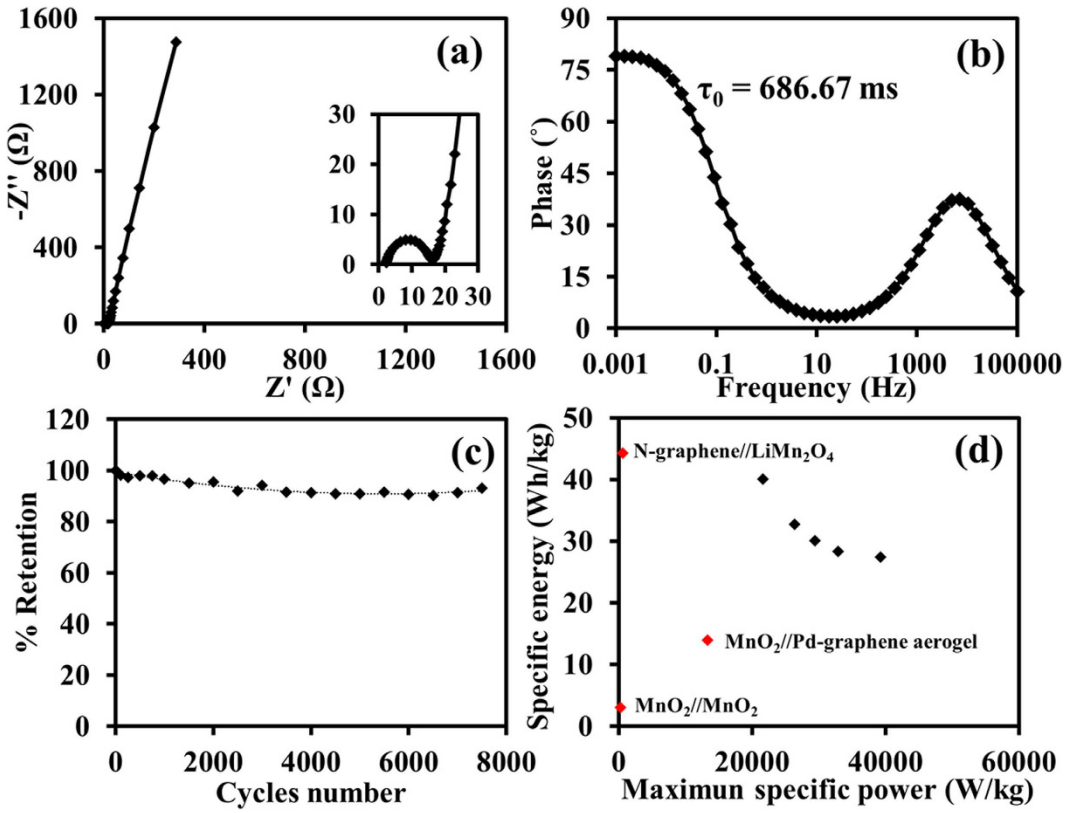

Figure 5. (**a**) Nyquist plot, (**b**) phase vs. frequency, (**c**) capacitance retention over 7,500 cycles, and (**d**) Ragone plots of the MnO_2//N-rGO_{ae} supercapacitor compared with other previous work[49-51].

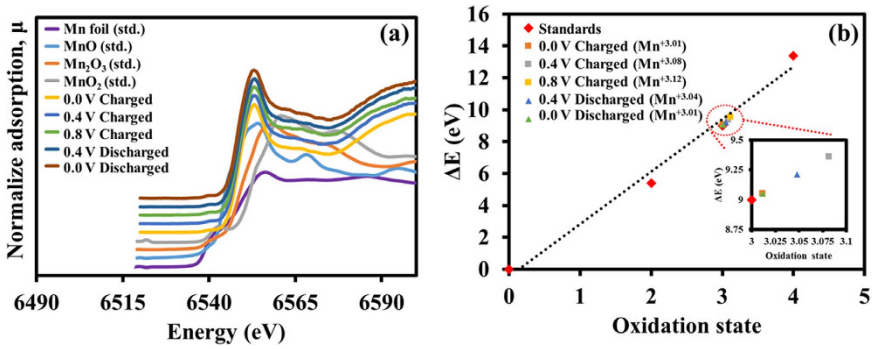

Figure 6. (**a**) *In situ* high-resolution Mn K-edge fluorescence XAS spectra of the as-prepared MnO_2 electrodes and Mn standard compounds and (**b**) the oxidation states vs. ΔE (eV) of the MnO_2 electrodes during charging/discharging by a chronoamperometry method at applied potentials from 0.0–0.8 V vs. SCE and backward potentials. Note, the XAS was carried out after reaching the steady state.

(see Fig. 6a). The Mn oxidation states of the MnO_2 electrode being charged at 0.0, 0.4, and 0.8 V vs. SCE are +3.01, +3.08, and +3.12, respectively (see Fig. 6b). Note, the oxidation number of the as-electrodeposited MnO_2 is +3.79.

The XAS result here confirms the reversible redox reaction of the MnO_2 and the proposed general redox reaction (4) below based on the intercalation/de-intercalation processes of Na^+ and H^+ is shown below[15,16,54,55];

$$MnO_a(OH)_b + xNa^+ + yH^+ + (x+y)e^- \leftrightarrow MnO_{a-x-y}(ONa_xH_y)_{b+x+y} \quad (4)$$

When the stepped potentials were applied backward from 0.8 to 0.4 V vs. SCE and afterward from 0.4 to 0.0 V vs. SCE, the edge energies are 6548.21 eV and 6548.05 eV, respectively (see Fig. 6a). The oxidation states of Mn in the MnO_2 return to +3.04 at 0.4 V vs. SCE and +3.01 at 0 V vs. SCE (see Fig. 6b).

In order to clarify the charge storage mechanism of the as-prepared K-birnessite MnO_2, the effect of the pH of 0.5 M Na_2SO_4 electrolyte was also studied by verying pH of the 0.5 M Na_2SO_4 electrolytes by adding conc. H_2SO_4

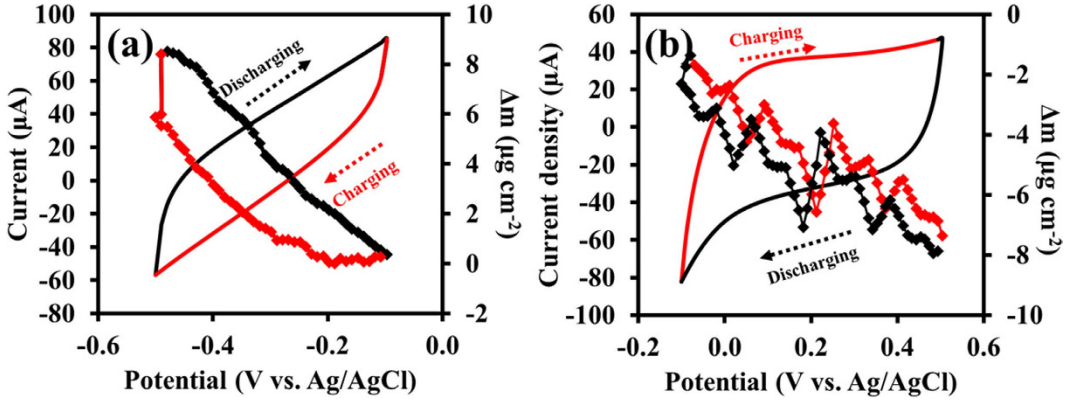

Figure 7. CVs at 25 mVs^{-1} and *in situ* EQCM responses of (**a**) N-rGO_{ae} and (**b**) MnO_2 electrodes.

(see the experimental results in Figure S5 and 6 of the supporting information). It is found that at pH beween 0.08 and 1.10, the solvated H^+ plays an important role in the charge storage capacity via an intercalation redox reaction (see redox peaks in CVs of Figure S5a) according to the reaction mechanism (5) below;

$$MnO_2 + H^+ + e^- \leftrightarrow MnOOH \quad (5)$$

At pH 2.03–4.02, the solvated Na^+ plays a major role to the charge storage capacity of the MnO_2 (see the mechanism in reaction (4) above). At pH > 5.36 adjusted by adding NaOH, it was found that the specific capacitances are significantly reduced since the MnO_2 layers having negative charge do not like to adsorb/absorb solvated anions i.e., OH^-. As the results, we can conclude that H^+ plays a significant role in the charge storage capacity at pH < 2.03.

Electrochemical quartz crystal microbalance. In addition to the *in situ* XAS results, the *in situ* gravimetric measurement of the mass changes on N-rGO_{ae} and MnO_2 electrodes was eventually evaluated via the EQCM method. The EQCM electrode was prepared by a drop-coating of the as-prepared materials onto the Au/TiO_2 quartz crystal surfaces. The *in situ* probing via the CV method was carried out in 0.5 M Na_2SO_4 solution using a three-electrode system with Ag/AgCl (3 M KCl) as the reference electrode and Au wire as the counter electrode (Fig. 7). The quartz resonance frequency (Δf) can be converted into the mass change (Δm) according to the derived Sauerbrey equation (6)[56] below;

$$\Delta f = -\Delta m C_f \quad (6)$$

where the frequency (Δf) in Hz and the calibration constant (C_f) is 0.0815 Hz $ng^{-1}cm^2$.

The CV and Δm from the quartz frequency response of N-rGO_{ae} are shown in Fig. 7a from −0.1 V to −0.5 V vs. Ag/AgCl. The CV shows a narrow potential window (about 0.6 V) because of small amount of N-rGO_{ae} coated onto the Au/TiO_2 electrode[57]. For the charge storage mechanisms of the N-rGO_{ae} at the negative electrode, it can store ionic charges via the physical adsorption (EDLC) at the solid-liquid interface by adsorbing/absorbing the solvated ions[58]. Furthermore, the N-containing groups of the N-doped rGO can store electronic charges via the redox reaction (7) below[58];

$$-CH = NH + 2e^- + H_2O \leftrightarrow -CH - NHOH \quad (7)$$

The Δm or mass deposited to the electrode during the charge process gradually increases to 8.4 μg cm^{-2}. After discharged, the ion accumulation releases to the electrolyte and the electrode returns to the initial state. Besides, the CV of the MnO_2 electrode in Fig. 7b displays an anodic potential range from −0.1 to 0.5 V vs. Ag/AgCl. The Δm is 7.4 μg cm^{-2}, relating to solvated cations (i.e. Na^+ and K^+) inserted/released from the MnO_2 layers. This is why the Mn oxidation state of the MnO_2 electrode being charged is increased. After fully discharged, the Δm returns to the initial value again confirming the XAS result.

Conclusions

High-performance asymmetric supercapacitor of the MnO_2//N-rGO_{ae} has been successfully fabricated. The MnO_2 nanosheets were prepared using a potential step electrodeposition and used as the positive electrode of the supercapacitor. The N-rGO_{ae} was synthesized using a hydrothermal process by reducing graphene oxide with hydrazine (a nitrogen source) and used as the negative electrode. The *in situ* XAS carried out together with the chronoamperometry indicates that the oxidation state of manganese ions in the MnO_2 electrode being charged remarkably rises from +3.01 to +3.12 when applying potentials at 0 to 0.8 V vs. SCE and returns to +3.01 at 0 V vs. SCE during the discharge process. This is a reason why MnO_2 nanosheets exhibit excellent capacity retention. The mass changes of solvated ions at the N-rGO_{ae}- and MnO_2-coated Au/TiO_2 quartz crystal EQCM electrodes during the charge/discharge processes are ca. 8.4 and 7.4 μg cm^{-2}, respectively. It is also found in this work that $[H^+]$ plays a significant role in the charge storage capacity at pH of the electrolyte, 0.5 M Na_2SO_4(aq) <2.03. At pH 2.03–4.02, the solvated Na^+ plays a major role to the charge storage capacity of the MnO_2. At pH > 5.36, the

specific capacitance of the device is significantly reduced since the birnassite MnO_2 layers having negative charge do not like to adsorb/absorb solvated anions i.e., OH^-. An as-fabricated MnO_2//N-rGO_{ae} with a finely tuned mass loading ratio of 1.75 provides a wide working potential of 1.6 V with the highest specific power and energy of 39 kW kg^{-1} and 40 Wh kg^{-1}, respectively. This device with a CR2016 size has 93.2% capacity retention after 7,500 cycles at 5 A g^{-1}. The enhancement in the specific energy and specific power of the MnO_2//N-rGO_{ae} supercapacitors can compete with the batteries in many applications.

Methods

Preparation of flexible carboxyl-modified carbon fiber paper (c-CFP). The c-CFP substrate was prepared by an acid treatement[13,29]. Briefly, conc. H_2SO_4 (150 ml) and conc. HNO_3 (50 ml) were mixed together in a beaker by stirring at 100 rpm for 10 min. The CFP with 5×5 cm^2 was then immersed to the acid mixture and kept stirring at 60 °C at 100 rpm for 1 h. The c-CFP was then washed with Milli-Q water 5 times and dried at 50 °C for 24 h.

Preparation of N-rGO_{ae} negative electrode. GO was firstly synthesized using a modified Hummers method previously reported by our group[14,26,59–62]. The N-rGO_{ae} was then synthesized via a hydrothermal reduction of GO with 0.5 M hydrazine (N_2H_4) a reducing agent. First, the as-synthesized GO (160 mg) was dispersed in Milli-Q water (80 ml) using a sonication process (100 w) for 2 h. N_2H_4 was then added to the mixture at room temperature. The mixture was consequently transferred to a Teflon autoclave (100 ml) and heated at 110 °C for 24 h to form N-rGO hydrogel. For the purification, the as-synthesized hydrogel was immersed in Milli-Q water to remove the residuals for 72 h. Finally, the hydrogel was frozen at 0 °C for 24 h. Then, the frozen hydrogel was put in a freezing dryer to remove water at −55 °C for 48 h. The product is so-called N-rGO_{ae}. In order to fabricate the negative electrode, the as-synthesized N-rGO_{ae} (3 mg) was dispersed in ethanol (3 ml), spray-coated on the c-CFP using an airbrush with a 0.3-mm brush nozzle (Paasche Airbrush Company, USA) and eventually dried at 50 °C for 24 h.

Potential-step electrodeposition of the MnO_2 positive electrode. The c-CFP at a diameter of 1.58 cm was immersed in an electrodeposition solution, 30 ml of 250 mM $Mn(NO_3)_2{\cdot}H_2O$ in 250 mM KCl. MnO_2 nanosheets were electrodeposied on the c-CFP by a potential-step electrodeposition at 1.0 V vs. SCE for 3 min and then suddenly switched to 0.5 V vs. SCE for 1 min for which a chronoamporometry method was carried out using a potentiostat (PGSTAT 302 N). In order to have 1–2 mg of MnO_2, this process was repeated for 10 times. Finally, the as-electrodeposited electrode was then washed 3 times with Milli-Q water to remove the residual KCl and dried at 50 °C for 24 h.

Morphological and structural characterizations. X-ray diffraction (XRD) using a D8 ADVANCE with DAVINCI design (Bruker optics, Germany) with CuK_α of 1.5418 Å was used to characterize the crystalline structures of the as-synthesised materials i.e., GO, N-rGO_{ae}, and MnO_2. The data were collected from 5 to 80° (2θ) with 0.01 increment. Note, the Si wafer was used as a holder for XRD measurement. Raman spectroscopy was also carried out using a laser excitation wavelength of 532 nm (Senterra Dispersive Raman, Bruker optics, Germany). The field-emission scanning electron microscopy (FE-SEM) images of the as-prepared materials were performed with an accelerating voltage of 15.0 kV (JSM-7001F, JEOL Ltd., Japan). The samples were mounted on the clean surface of carbon conductive tab and placing on the SEM pin stub. Note that the specimens were coated with the platinum by a sputtering technique for 40 sec in order to remove the charging effect. The transmission electron microscopy (TEM) images of the samples were performed with an accelerating voltage of 100 kV (a JEM 1220, JEOL Ltd., Japan). The TEM specimens were prepared by dropping the suspension (~0.05 mg/ml) of N-rGO_{ae}, and MnO_2 in ethanol in the copper grids and dried at 50 °C for 3 h. The functional groups and elemental compositions of the as-synthesised materials were also analyzed by X-ray photoelectron spectroscopy (XPS) using an AXIS Ultra DLD (Kratos Analytical Ltd., Manchester, UK) with Al-K alpha radiation ($h\nu = 14{,}866$ eV). In addition, *in situ* Mn K-edge fluorescent x-ray photoelectron spectroscopy (XAS) measurement was performed at a beamline No. 5 at the Synchrotron Light Research Institute (Public Organization), Nakhon Ratchasima, Thailand using a Ge(220) double-crystal monochromator (energy range 3440–12100 eV). The spectroscopic data were collected in fluorescence mode with a 4-element silicon drift detector. The 4-element silicon drift detector was placed 90° to the beam and 45° to the sample. The Mn K-edge (6539 eV) was calibrated using the Mn foil before measurement. The light dimension on the sample was adjusted to 5 mm width and 1 mm height. The advantage of using *in situ* XAS measurements is that it can probe or localize the Mn element of the MnO_2 electrode during charging/discharging.

For the *in situ* electrochemical XAS measurement, a chronoamperometry method was used at different potentials (i.e., 0, 0.4, and 0.8 V vs. SCE) to evaluate the electrochemical property of the electrodes. In this measurement, a 3-electrode system using SCE as a reference electrode, Pt wire as a counter electrode, and the as-prepared MnO_2 working electrode was carried out in a 0.5 M Na_2SO_4 (aq.) electrolyte. Note, the electrochemical cell was made from acrylic sheets with the dimension of $2 \times 2 \times 3.5$ cm^3 having a drilled hole diameter of 0.8 cm on one 2-cm^2 side of the acrylic sheet. The drilled hole was covered by a larger piece of Kapton tape with a diameter of 1.2 cm. The SCE and Pt wire were placed beside the MnO_2 electrode at a distance of ca.1 cm but away from the path of the X-rays. In order to get a steady-state current, the MnO_2 working electrode was kept at a given potential of interest for at least 15 min before the *in situ* XAS and chronoamperometry measurements.

Fabrication of ASCs and the electrochemical evaluation. The ASCs were assembled of the negative and positive electrodes with a coin-cell size (CR2016). Hydrolyzed polyethylene (PE) film with a thickness of 25 μm was used as the separator of aqueous-based supercapacitors and 0.5 M Na_2SO_4(aq) was used as the electrolyte. The electrolyte seperator was prepared by soaking the hydrolized PE in 0.5 M Na_2SO_4(aq) for 10 min before

assembled. Then, the separator was inserted betweent positive and negative electrode. Finally, the coin cell was then assembled by pressing with crimper machine at 100 psi. The electrochemical evaluation of the as-fabricated supercapacitors was carried out using a Metrohm AUTOLAB potentiostat (PGSTAT 302 N) made in Netherlands running NOVA software (version 1.11). Cyclic voltammetry (CV), galvanostatic charge–discharge (GCD), and electrochemical impedance spectroscopy (EIS) were performed.

Calculation of supercapacitor performances. The specific capacitance (C_{cv}) of the supercapacitor cell excluding the influence of the c-CFP substrate can be determined from the CV by following calculation Eq. (8)[40,63–65].

$$C_{cv} = 4\int \frac{IdV/v}{m\Delta V} \tag{8}$$

where ΔV is the working potential determined from the discharge potential chosen in the potential range without H_2 and O_2 evolution, IdV is an area under the discharging curve, v is a scan rate (V/s), and m is a total active mass at negative and positive electrodes (g).

The specific capacitance can also be calculated from the GCD method (C_{GCD}) by following Eq. (9)[40,65,66];

$$G_{GCD} = 4\left(\frac{I\Delta t}{\Delta V_{cell} m_{total}}\right) \tag{9}$$

where I is the applied constant current (A), Δt is the discharging time (s), and ΔV_{cell} is the potential window (V) excluding iR drop. Note, the iR drop increases when increasing the applied current rate.

The specific capacitance determined from the EIS technique (C_{EIS}) can be calculated from Eq. (10)[2,67,68];

$$\mathrm{C_{EIS}} = 4\left(\frac{-1}{2\pi \mathrm{f} Z'' \mathrm{m_{total}}}\right) \tag{10}$$

where f is the applied frequency and Z'' is the imaginary component of the impedance at the frequency f, which is a negative value. In addition, the equivalent series resistance (ESR) of the supercapacitors was simply determined from the intercept at the X-axis of the Nyquist plots.

Besides, the specific energy (E) of the supercapacitors were calculated by following Eq. (11)[69–71];

$$E = \frac{1}{2} C_{cell} V_{cell}^2 \tag{11}$$

The maximum power (P_{max}) at the discharge efficiency of 50% from a maximum voltage at the fully charged state can be calculated as the following Eq. (12)[69] ;

$$P_{max} = \frac{V_{max}^2}{4R_{cell}} \tag{12}$$

where V_{max} is a maximum voltage of the cell, and R_{cell} is a resistance of the cell, which can be determined from the iR_{cell} drop observed in the GCD[13].

References

1. Pech, D. *et al.* Ultrahigh-power micrometre-sized supercapacitors based on onion-like carbon. *Nat. Nanotechnol.* **5,** 651–654 (2010).
2. Wang, X. *et al.* Three-dimensional strutted graphene grown by substrate-free sugar blowing for high-power-density supercapacitors. *Nat. Commun.* **4,** doi: 10.1038/ncomms3905 (2013).
3. Pandolfo, A. G. & Hollenkamp, A. F. Carbon properties and their role in supercapacitors. *J. Power Sources* **157,** 11–27 (2006).
4. Liu, C., Yu, Z., Neff, D., Zhamu, A. & Jang, B. Z. Graphene-Based Supercapacitor with an Ultrahigh Energy Density. *Nano Lett.* **10,** 4863–4868 (2010).
5. Kotz, R. & Carlen, M. Principles and applications of electrochemical capacitors. *Electrochim. Acta* **45,** 2483–2498 (2000).
6. Fan, Z. *et al.* Asymmetric Supercapacitors Based on Graphene/MnO_2 and Activated Carbon Nanofiber Electrodes with High Power and Energy Density. *Adv. Funct. Mater.* **21,** 2366–2375 (2011).
7. Dubal, D. P. *et al.* Synthetic approach from polypyrrole nanotubes to nitrogen doped pyrolyzed carbon nanotubes for asymmetric supercapacitors. *J. Power Sources* **308,** 158–165 (2016).
8. Ma, H. *et al.* Nickel Cobalt Hydroxide @Reduced Graphene Oxide Hybrid Nanolayers for High Performance Asymmetric Supercapacitors with Remarkable Cycling Stability. *Acs App. Mater. Interfaces* **8,** 1992–2000 (2016).
9. Yu, N. *et al.* High-Performance Fiber-Shaped All-Solid-State Asymmetric Supercapacitors Based on Ultrathin MnO_2 Nanosheet/Carbon Fiber Cathodes for Wearable Electronics. *Adv.Energy Mater.* **6,** doi: 10.1002/aenm.201501458 (2016).
10. Zhu, C. *et al.* All Metal Nitrides Solid-State Asymmetric Supercapacitors. *Adv. Mater.* **27,** 4566–4571 (2015).
11. Zeng, Y. *et al.* Advanced Ti-Doped Fe_2O_3@PEDOT Core/Shell Anode for High-Energy Asymmetric Supercapacitors. *Adv.Energy Mater.* **5,** doi: 10.1002/aenm.201402176 (2015).
12. Phattharasupakun, N. *et al.* Turning conductive carbon nanospheres into nanosheets for high-performance supercapacitors of MnO_2 nanorods. *Chem. Commun.* **52,** 2585–2588 (2016).
13. Suktha, P. *et al.* High-Performance Supercapacitor of Functionalized Carbon Fiber Paper with High Surface Ionic and Bulk Electronic Conductivity: Effect of Organic Functional Groups. *Electrochim. Acta* **176,** 504–513 (2015).
14. Sawangphruk, M. *et al.* High-performance supercapacitor of manganese oxide/reduced graphene oxide nanocomposite coated on flexible carbon fiber paper. *Carbon* **60,** 109–116 (2013).
15. Lang, X., Hirata, A., Fujita, T. & Chen, M. Nanoporous metal/oxide hybrid electrodes for electrochemical supercapacitors. *Nat. Nanotechnol.* **6,** 232–236 (2011).
16. Lee, H. Y. & Goodenough, J. B. Supercapacitor Behavior with KCl Electrolyte. *J. Solid State Chem.* **144,** 220–223 (1999).

17. Toupin, M., Brousse, T. & Bélanger, D. Charge Storage Mechanism of MnO2 Electrode Used in Aqueous Electrochemical Capacitor. *Chem. Mater*. **16,** 3184–3190 (2004).
18. Xu, C., Wei, C., Li, B., Kang, F. & Guan, Z. Charge storage mechanism of manganese dioxide for capacitor application: Effect of the mild electrolytes containing alkaline and alkaline-earth metal cations. *J. Power Sources* **196,** 7854–7859 (2011).
19. Chen, D. *et al.* Probing the Charge Storage Mechanism of a Pseudocapacitive MnO2 Electrode Using in Operando Raman Spectroscopy. *Chem. Mater*. **27,** 6608–6619 (2015).
20. Yang, J. *et al.* All-Solid-State High-Energy Asymmetric Supercapacitors Enabled by Three-Dimensional Mixed-Valent MnOx Nanospike and Graphene Electrodes. *ACS App. Mater. Interfaces* **7,** 22172–22180 (2015).
21. Hu, C.-C., Hung, C.-Y., Chang, K.-H. & Yang, Y.-L. A hierarchical nanostructure consisting of amorphous MnO_2, Mn_3O_4 nanocrystallites, and single-crystalline MnOOH nanowires for supercapacitors. *J. Power Sources* **196,** 847–850 (2011).
22. Hu, Y. & Wang, J. MnOx nanosheets for improved electrochemical performances through bilayer nano-architecting. *J. Power Sources* **286,** 394–399 (2015).
23. Li, Y. *et al.* Manganese oxide nanowires wrapped with nitrogen doped carbon layers for high performance supercapacitors. *J. Colloid Interface Sci.* **455,** 188–193 (2015).
24. Ali, G. A. M., Yusoff, M. M., Ng, Y. H., Lim, H. N. & Chong, K. F. Potentiostatic and galvanostatic electrodeposition of manganese oxide for supercapacitor application: A comparison study. *Cur. App. Phys*. **15,** 1143–1147 (2015).
25. Qin, Y.-H. *et al.* Electrophoretic deposition of network-like carbon nanofibers as a palladium catalyst support for ethanol oxidation in alkaline media. *Carbon* **48,** 3323–3329 (2010).
26. Iamprasertkun, P., Krittayavathananon, A. & Sawangphruk, M. N-doped reduced graphene oxide aerogel coated on carboxyl-modified carbon fiber paper for high-performance ionic-liquid supercapacitors. *Carbon* **102,** 455–461 (2016).
27. You, B., Wang, L., Yao, L. & Yang, J. Three dimensional N-doped graphene-CNT networks for supercapacitor. *Chem. Commun.* **49,** 5016–5018 (2013).
28. Lee, Y.-H., Chang, K.-H. & Hu, C.-C. Differentiate the pseudocapacitance and double-layer capacitance contributions for nitrogen-doped reduced graphene oxide in acidic and alkaline electrolytes. *J. Power Sources* **227,** 300–308 (2013).
29. Kaewsongpol, T. *et al.* High-performance supercapacitor of electrodeposited porous 3D polyaniline nanorods on functionalized carbon fiber paper: Effects of hydrophobic and hydrophilic surfaces of conductive carbon paper substrates. *Mater. Today Commun*. **4,** 176–185 (2015).
30. Srimuk, P., Luanwuthi, S., Krittayavathananon, A. & Sawangphruk, M. Solid-type supercapacitor of reduced graphene oxide-metal organic framework composite coated on carbon fiber paper. *Electrochim. Acta* **157,** 69–77 (2015).
31. Yin, F. *et al.* Self-assembly of mildly reduced graphene oxide monolayer for enhanced Raman scattering. *J. Solid State Chem.* **237,** 57–63 (2016).
32. Ji, C.-C. *et al.* Self-assembly of three-dimensional interconnected graphene-based aerogels and its application in supercapacitors. *J. Colloid Interface Sci.* **407,** 416–424 (2013).
33. Sui, Z.-Y. *et al.* Nitrogen-Doped Graphene Aerogels as Efficient Supercapacitor Electrodes and Gas Adsorbents. *ACS App. Mater. Interfaces* **7,** 1431–1438 (2015).
34. Zhang, X. *et al.* Rapid hydrothermal synthesis of hierarchical nanostructures assembled from ultrathin birnessite-type MnO_2 nanosheets for supercapacitor applications. *Electrochim. Acta* **89,** 523–529 (2013).
35. Dubal, D. P. *et al.* 3D hierarchical assembly of ultrathin MnO_2 nanoflakes on silicon nanowires for high performance micro-supercapacitors in Li- doped ionic liquid. *Sci. Rep*. **5,** 9771 (2015).
36. Julien, C. *et al.* Raman spectra of birnessite manganese dioxides. *Solid State Ion.* **159,** 345–356 (2003).
37. Some, S., Kim, Y., Hwang, E., Yoo, H. & Lee, H. Binol salt as a completely removable graphene surfactant. *Chem. Commun.* **48,** 7732–7734 (2012).
38. Liu, Y., He, D., Wu, H., Duan, J. & Zhang, Y. Hydrothermal Self-assembly of Manganese Dioxide/Manganese Carbonate/Reduced Graphene Oxide Aerogel for Asymmetric Supercapacitors. *Electrochim. Acta* **164,** 154–162 (2015).
39. Fan, W., Miao, Y.-E., Huang, Y., Tjiu, W. W. & Liu, T. Flexible free-standing 3D porous N-doped graphene-carbon nanotube hybrid paper for high-performance supercapacitors. *RSC Adv*. **5,** 9228–9236 (2015).
40. Béguin, F., Presser, V., Balducci, A. & Frackowiak, E. Carbons and Electrolytes for Advanced Supercapacitors. *Adv. Mater.* **26,** 2219–2251 (2014).
41. Liang, M., Liu, X., Li, W. & Wang, Q. A Tough Nanocomposite Aerogel of Manganese Oxide and Polyaniline as an Electrode for a Supercapacitor. *ChemPlusChem* **81,** 40–43 (2016).
42. Wang, H.-Q. *et al.* Direct growth of flower-like 3D MnO_2 ultrathin nanosheets on carbon paper as efficient cathode catalyst for rechargeable Li-O_2 batteries. *RSC Adv*. **5,** 72495–72499 (2015).
43. Chen, H. *et al. In situ* growth of NiCo2S4 nanotube arrays on Ni foam for supercapacitors: Maximizing utilization efficiency at high mass loading to achieve ultrahigh areal pseudocapacitance. *J. Power Sources* **254,** 249–257 (2014).
44. Wang, R., Xu, C. & Lee, J.-M. High performance asymmetric supercapacitors: New NiOOH nanosheet/graphene hydrogels and pure graphene hydrogels. *Nano Energy* **19,** 210–221 (2016).
45. Sathiya, M., Prakash, A. S., Ramesha, K., Tarascon, J. M. & Shukla, A. K. V2O5-Anchored Carbon Nanotubes for Enhanced Electrochemical Energy Storage. *J. Am. Chem. Soc.* **133,** 16291–16299 (2011).
46. Augustyn, V., Simon, P. & Dunn, B. Pseudocapacitive oxide materials for high-rate electrochemical energy storage. *Energy Environ. Sci.* **7,** 1597–1614 (2014).
47. Lee, G. *et al.* High-performance all-solid-state flexible micro-supercapacitor arrays with layer-by-layer assembled MWNT/MnOx nanocomposite electrodes. *Nanoscale* **6,** 9655–9664 (2014).
48. Yuan, L. *et al.* Flexible Solid-State Supercapacitors Based on Carbon Nanoparticles/MnO2 Nanorods Hybrid Structure. *ACS Nano* **6,** 656–661 (2012).
49. Yu, Z. *et al.* Functionalized graphene aerogel composites for high-performance asymmetric supercapacitors. *Nano Energy* **11,** 611–620 (2015).
50. Yang, X. *et al.* High-performance aqueous asymmetric supercapacitor based on spinel LiMn2O4 and nitrogen-doped graphene/porous carbon composite. *Electrochim. Acta* **180,** 287–294 (2015).
51. Kalubarme, R. S., Jadhav, H. S. & Park, C.-J. Electrochemical characteristics of two-dimensional nano-structured MnO_2 for symmetric supercapacitor. *Electrochim. Acta* **87,** 457–465 (2013).
52. Wongsaprom, K., Sonsupap, S., Maensiri, S. & Kidkhunthod, P. Room-temperature ferromagnetism in Fe-doped In_2O_3 nanoparticles. *App. Phys. A* **121,** 239–244 (2015).
53. Daengsakul, S. *et al.* The effect of Gd doping in $La1-x-yGdxSryMnO_3$ compound on nanocrystalline structure by X-ray Absorption Spectroscopy (XAS) technique. *Microelectron. Eng.* **146,** 38–42 (2015).
54. Ghaemi, M., Ataherian, F., Zolfaghari, A. & Jafari, S. M. Charge storage mechanism of sonochemically prepared MnO2 as supercapacitor electrode: Effects of physisorbed water and proton conduction. *Electrochimica Acta* **53,** 4607–4614 (2008).
55. Simon, P. & Gogotsi, Y. Materials for electrochemical capacitors. *Nat. Mater.* **7,** 845–854 (2008).
56. Sauerbrey, G. Verwendung von Schwingquarzen zur Wägung dünner Schichten und zur Mikrowägung. *Z. Phys*. **155,** 206–222 (1959).
57. Tsai, W.-Y., Taberna, P.-L. & Simon, P. Electrochemical Quartz Crystal Microbalance (EQCM) Study of Ion Dynamics in Nanoporous Carbons. *J. Am. Chem. Soc.* **136,** 8722–8728 (2014).

58. Yan, J. *et al.* Advanced Asymmetric Supercapacitors Based on Ni(OH)2/Graphene and Porous Graphene Electrodes with High Energy Density. *Adv. Funct. Mater.* **22,** 2632–2641 (2012).
59. Hummers, W. S. & Offeman, R. E. Preparation of Graphitic Oxide. *J. Am. Chem. Soc.* **80,** 1339–1339 (1958).
60. Luanwuthi, S., Krittayavathananon, A., Srimuk, P. & Sawangphruk, M. *In situ* synthesis of permselective zeolitic imidazolate framework-8/graphene oxide composites: rotating disk electrode and Langmuir adsorption isotherm. *RSC Adv.* **5,** 46617–46623 (2015).
61. Sanguansak, Y. *et al.* Permselective properties of graphene oxide and reduced graphene oxide electrodes. *Carbon* **68,** 662–669 (2014).
62. Krittayavathananon, A., Iamprasertkun, P. & Sawangphruk, M. Enhancing the charge-storage performance of N-doped reduced graphene oxide aerogel supercapacitors by adsorption of the cationic electrolytes with single-stand deoxyribonucleic acid. *Carbon* **109,** 314–320 (2016).
63. McDonough, J. K. *et al.* Influence of the structure of carbon onions on their electrochemical performance in supercapacitor electrodes. *Carbon* **50,** 3298–3309 (2012).
64. Lu, Y. *et al.* Hierarchical, porous CuS microspheres integrated with carbon nanotubes for high-performance supercapacitors. *Scientific Reports* **5,** 16584 (2015).
65. Yang, J. *et al.* Rapid and controllable synthesis of nitrogen doped reduced graphene oxide using microwave-assisted hydrothermal reaction for high power-density supercapacitors. *Carbon* **73,** 106–113 (2014).
66. Singh, A. & Chandra, A. Significant Performance Enhancement in Asymmetric Supercapacitors based on Metal Oxides, Carbon nanotubes and Neutral Aqueous Electrolyte. *Sci. Rep.* **5,** 15551 (2015).
67. Tooming, T., Thomberg, T., Kurig, H., Jänes, A. & Lust, E. High power density supercapacitors based on the carbon dioxide activated d-glucose derived carbon electrodes and 1-ethyl-3-methylimidazolium tetrafluoroborate ionic liquid. *J. Power Sources* **280,** 667–677 (2015).
68. Berton, N. *et al.* Wide-voltage-window silicon nanowire electrodes for micro-supercapacitors via electrochemical surface oxidation in ionic liquid electrolyte. *Electrochem. Commun.* **41,** 31–34 (2014).
69. Chu, A. & Braatz, P. Comparison of commercial supercapacitors and high-power lithium-ion batteries for power-assist applications in hybrid electric vehicles: I. Initial characterization. *J. Power Sources* **112,** 236–246 (2002).
70. Xiao, X. *et al.* Freestanding functionalized carbon nanotube-based electrode for solid-state asymmetric supercapacitors. *Nano Energy* **6,** 1–9 (2014).
71. Huang, P.-L. *et al.* Ionic Liquid Electrolytes with Various Constituent Ions for Graphene-based Supercapacitors. *Electrochim. Acta* **161,** 371–377 (2015).

Acknowledgements

Financial supports by Thailand Research Fund (TRF) and Vidyasirimedhi Institute of Science and Technology (VISTEC) are acknowledged (RSA5880043). This research is also supported in part by the Graduate Program Scholarship from the Graduate School, Kasetsart University. Supports from the Center of Excellence on Petrochemical and Materials Technology (PETROMAT), the Kasetsart University Research and Development Institute (KURDI), Department of Chemical Engineering, Kasetsart University, National Research University Project of Thailand (NRU), Synchrotron Light Research Institute (BL5.1 and BL5.2) (Public Organization), Thailand for XANES and XPS facilities, and the Frontier Research Center at VISTEC are also acknowledged.

Author Contributions

P.I. and A.K. synthesized the materials and performed the electrochemical experiment and discussed the results. M.S. designed and directed the work, discussed the results, and wrote the manuscript. N.C., P.K., W.S., S.N., P.P., and S.I. helped for the sample measurements including FTIR, RAMAN, XPS, XAS, SEM and TEM. A.S., S.M., R.Y., K.K., and J.L. discussed the results.

Additional Information

Supplementary information accompanies this paper at http://www.nature.com/srep

Competing financial interests: The authors declare no competing financial interests.

How to cite this article: Iamprasertkun, P. *et al.* Charge storage mechanisms of manganese oxide nanosheets and N-doped reduced graphene oxide aerogel for high-performance asymmetric supercapacitors. *Sci. Rep.* **6**, 37560; doi: 10.1038/srep37560 (2016).

Publisher's note: Springer Nature remains neutral with regard to jurisdictional claims in published maps and institutional affiliations.

This work is licensed under a Creative Commons Attribution 4.0 International License. The images or other third party material in this article are included in the article's Creative Commons license, unless indicated otherwise in the credit line; if the material is not included under the Creative Commons license, users will need to obtain permission from the license holder to reproduce the material. To view a copy of this license, visit http://creativecommons.org/licenses/by/4.0/

© The Author(s) 2016